**Supporting Information**

# Strong Inhibition of O-Atom Transfer Reactivity for $Mn^{IV}(O)(\pi\text{-radical-cation})(\text{Lewis acid})$ Versus $Mn^{V}(O)$ Porphyrinoid Complexes

*Jan Paulo T. Zaragoza, Regina A. Baglia, Maxime A. Siegler, and David P. Goldberg**

Department of Chemistry, The Johns Hopkins University, 3400 N. Charles Street, Baltimore, MD 21218, USA

*E-mail: dpg@jhu.edu

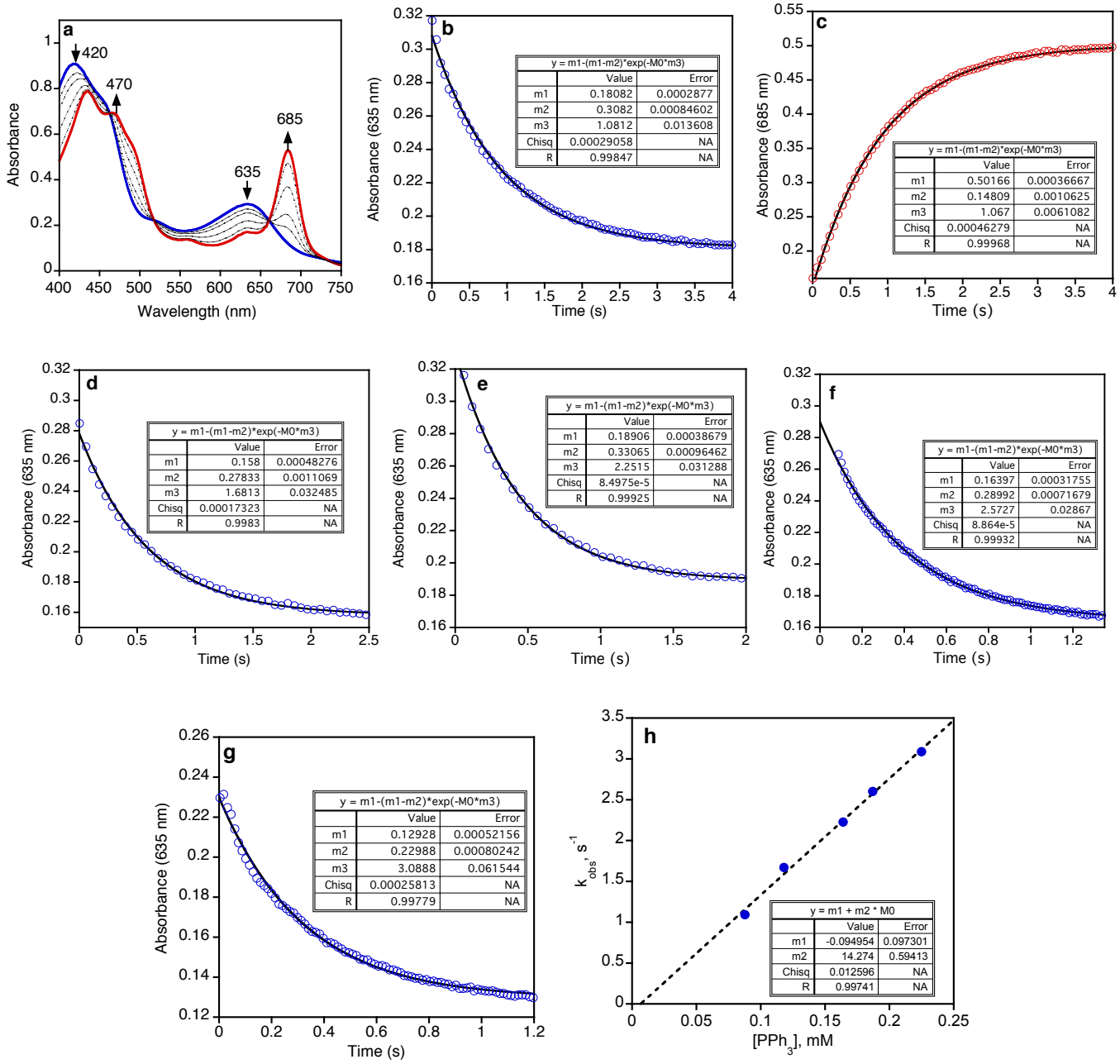


**Figure S1.** a) Stopped-flow UV-vis spectral changes (0 – 4 s) for the reaction of $Mn^{V}(O)(TBP_8Cz)$ (13 μM) (blue line) and $PPh_3$ (0.09 mM) forming $Mn^{III}(TBP_8Cz)$ (red line) in $CH_2Cl_2$ at 25˚C. b) Changes in absorbance at 635 nm over time following the decay of $Mn^{V}(O)(TBP_8Cz)$. c) Changes in absorbance at 685 nm over time following the growth of $Mn^{III}(TBP_8Cz)$. Changes in absorbance at 635 nm over time following the decay of $Mn^{V}(O)(TBP_8Cz)$ after addition of varying amounts of $PPh_3$: d) 0.12 mM, e) 0.16 mM, f) 0.19 mM, and g) 0.23 mM. h) Plot of $k_{obs}$ versus [$PPh_3$].

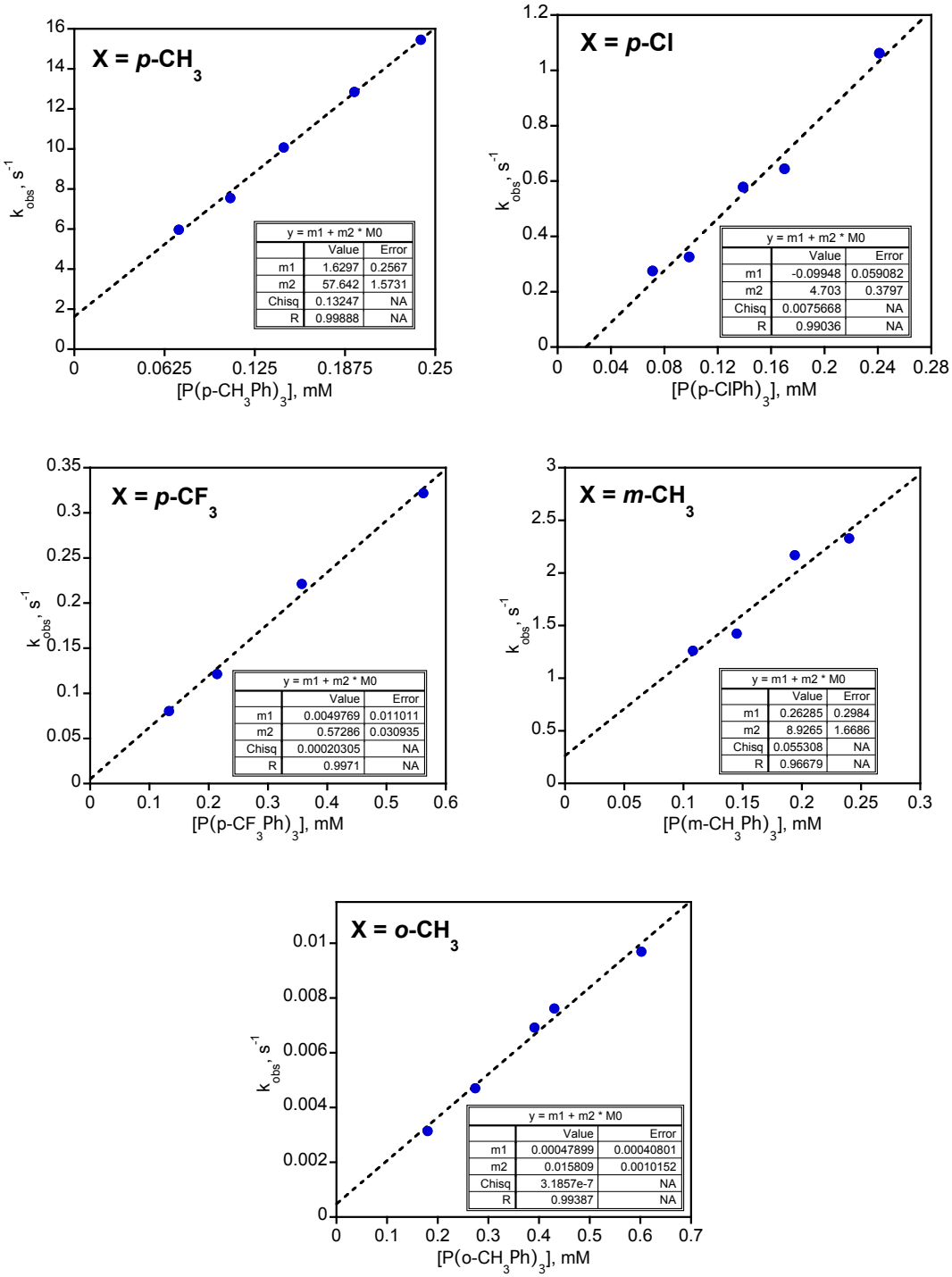


**Figure S2.** Plots of $k_{obs}$ versus $[P(X\text{-}Ph)_3]$ for the reaction of $Mn^V(O)(TBP_8Cz)$ (13 μM) in $CH_2Cl_2$ at 25˚C with substituted triarylphosphines: X = *p*-$CH_3$ (0.07 – 0.24 mM), *p*-Cl (0.07 – 0.24 mM), *p*-$CF_3$ (0.13 – 0.56 mM), *m*-$CH_3$ (0.11 – 0.24 mM), *o*-$CH_3$ (0.18 – 0.60 mM).

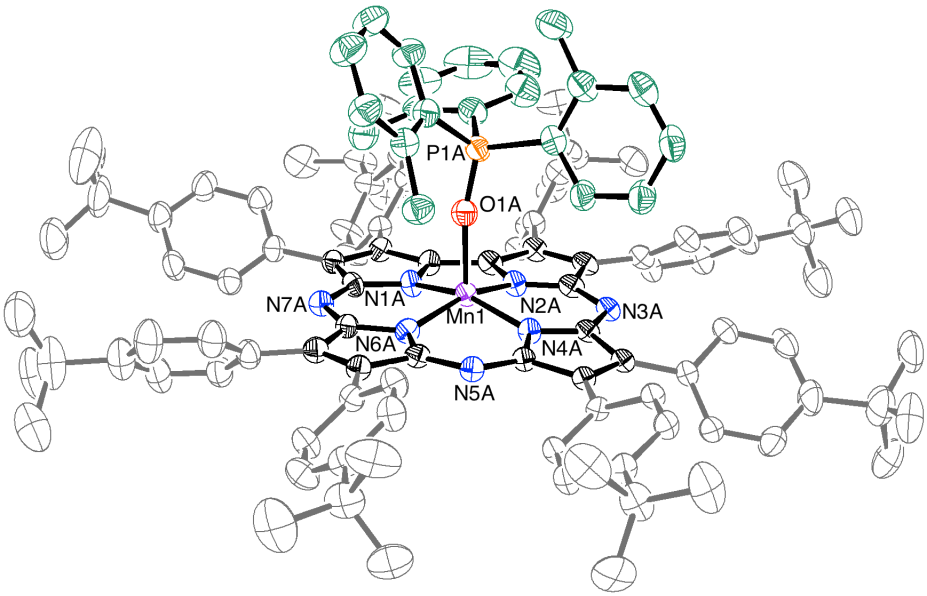


**Figure S3.** Displacement ellipsoid plot (50% probability level) of $Mn^{III}(OP(o\text{-tolyl})_3)(TBP_8Cz)$ (**2a**) at 110(2) K. The disorder, H atoms and solvent molecules are omitted for clarity.

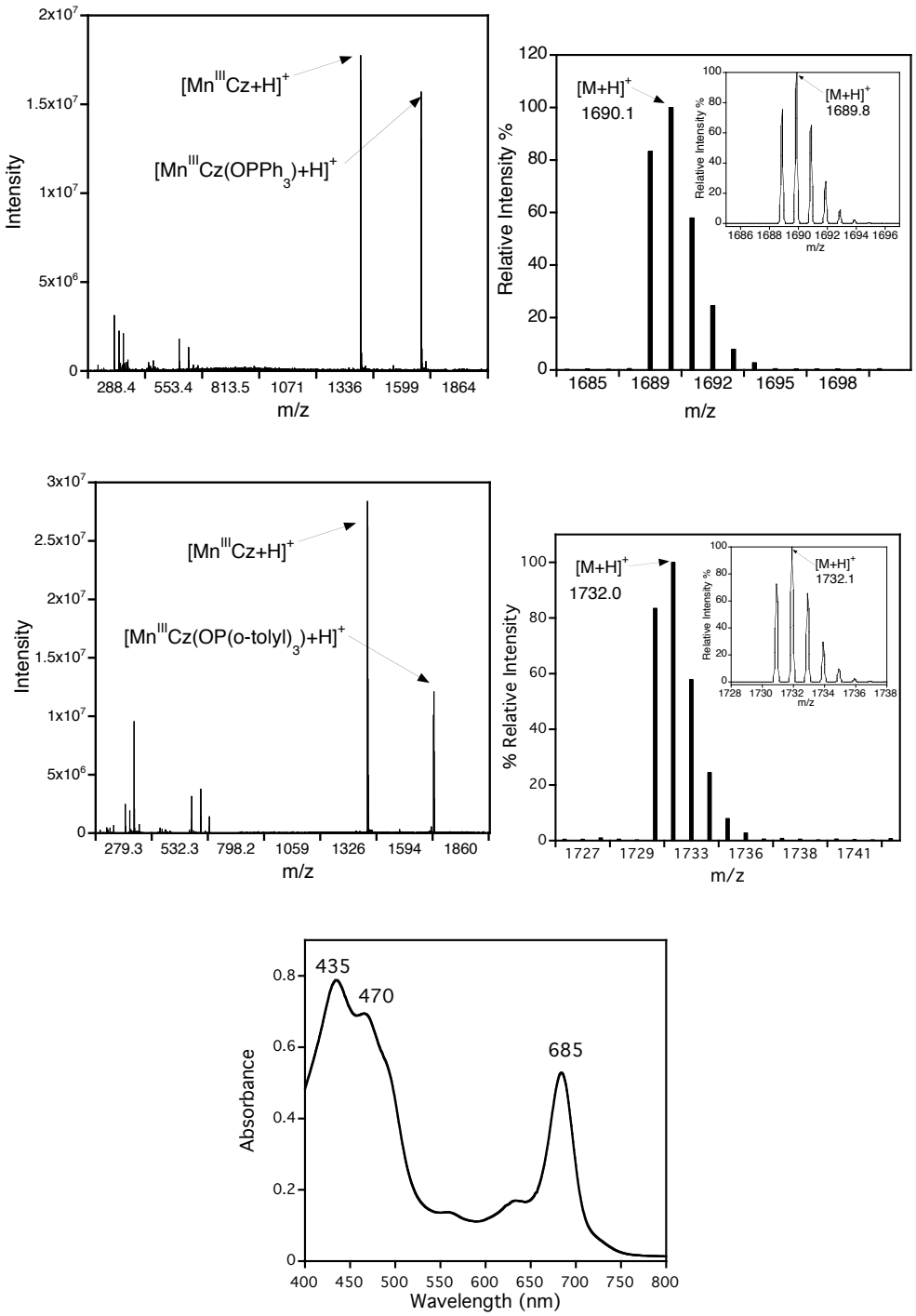


**Figure S4.** ESI-MS spectra and experimental isotope pattern for the $[M+H]^+$ peak (inset: calculated isotope pattern for the $[M+H]^+$ peak) for $Mn^{III}(OPPh_3)(TBP_8Cz)$ (top) and $Mn^{III}(OP(o\text{-tolyl})_3)(TBP_8Cz)$ (middle). UV-vis spectra of $Mn^{III}(OPPh_3)(TBP_8Cz)$ crystals in $CH_2Cl_2$ (bottom).

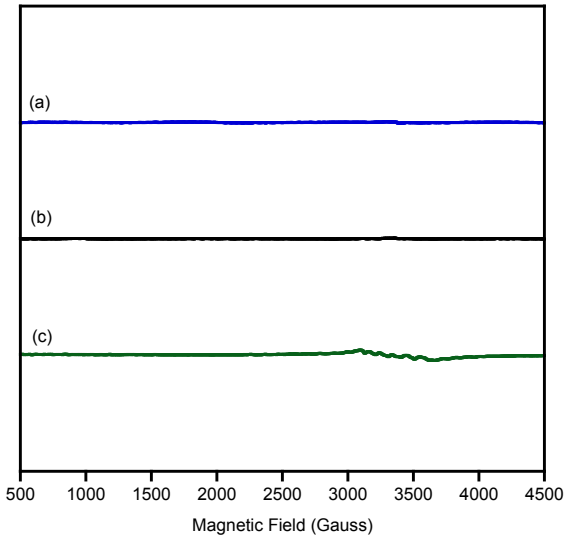


**Figure S5.** X-band EPR spectra for a) $Mn^{III}(TBP_8Cz)$ (2 mM) + $Zn(OTf)_2$ (2 equiv) in $CH_2Cl_2$:$CH_3CN$ (5:1 v/v), b) $Mn^{III}(TBP_8Cz)$ (2 mM) in $CH_2Cl_2$, c) $Mn^{IV}(O)(TBP_8Cz^{\bullet+})$:$Zn^{II}$ (2 mM) + 10 $PPh_3$ in $CH_2Cl_2$:$CH_3CN$ (25:1 v/v). EPR parameters: $T$ = 13 K, freq. = 9.448 GHz, power = 20.0 mW, mod. amp. = 10 G, mod. freq. = 100 kHz, receiver gain = 5.00 x $10^3$. Spectra were an average of 2 scans. The lack of an EPR signal in (a) and (b) is expected for an integer-spin $Mn^{III}$ ($S$ = 2) complex. A similar absence of an intense EPR signal is seen for (c), consistent with the $Mn^{III}$ product formed from the two-electron O-atom transfer reaction between $Mn^{IV}(O)(TBP_8Cz^{\bullet+})$:$Zn^{II}$ and $PPh_3$. The residual 6-line signal observed at $g$ = 2 in (c) is assigned to a minor $Mn^{II}$ impurity. This signal was previously observed upon decomposition of $Mn^{III}(TBP_8Cz)$ with a strong acid (HOTf), and has a characteristic hyperfine coupling constant of $A_{iso}(^{55}Mn)$ = 120 G.

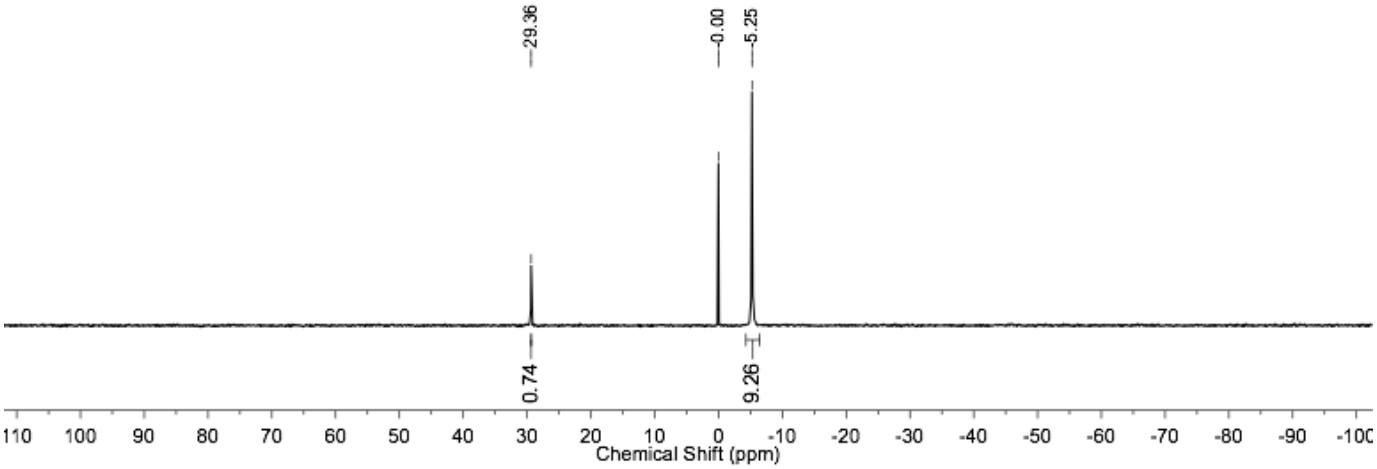


**Figure S6.** $^{31}P\{^1H\}$ NMR spectrum for the reaction mixture of $Mn^{IV}(O)(TBP_8Cz^{\bullet+})$:$Zn^{II}$ + 10 $PPh_3$ after addition of excess $Bu_4N^+F^-$ in $CD_2Cl_2$:$CD_3CN$ (10:1 v/v). Peaks for $PPh_3$ (δ = -5.2 ppm) and $OPPh_3$ (δ = 29.4 ppm) were observed, and chemical shifts were referenced to an external 85% $H_3PO_4$ standard (δ = 0 ppm). A yield of 74% for $OPPh_3$ was obtained by comparison of the integrations for $PPh_3$ and $OPPh_3$.

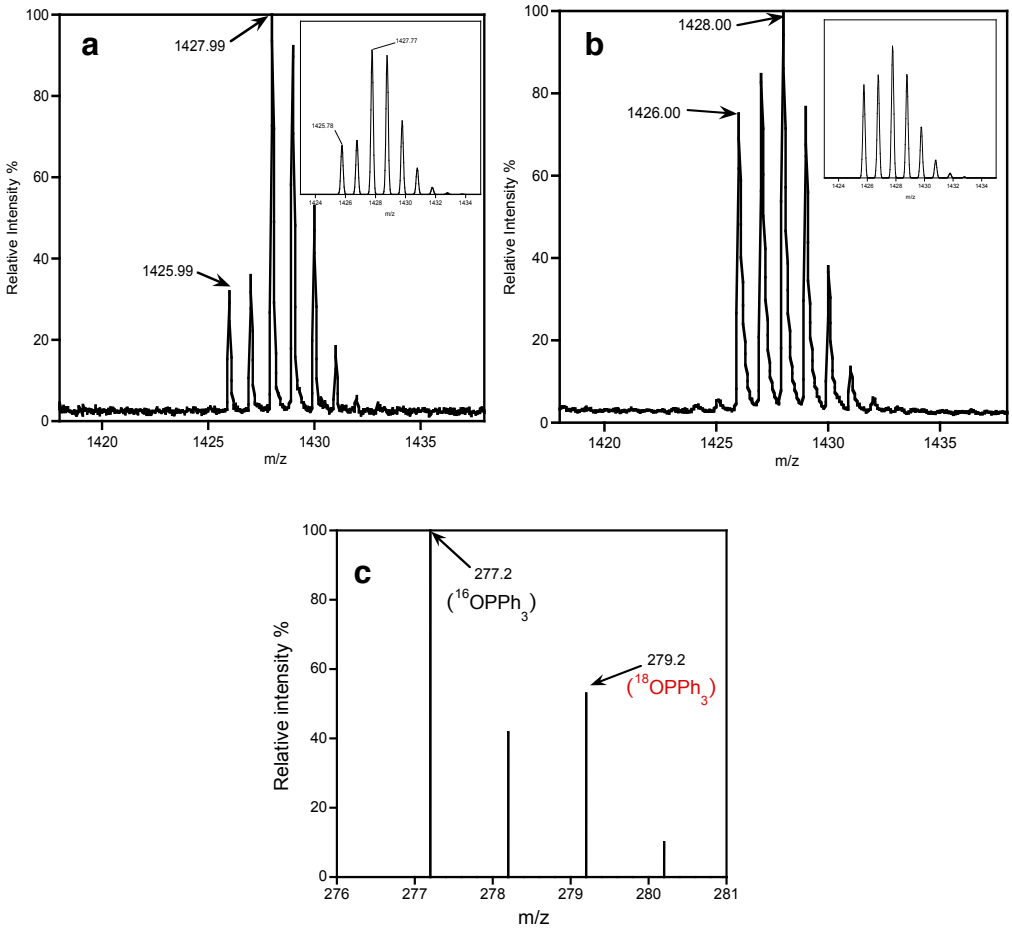


**Figure S7.** a) LDI-MS spectrum (positive ion mode) for $Mn^{V}(^{18}O)(TBP_8Cz)$ showing the isotope distribution pattern which corresponds to 70% incorporation of $^{18}O$. Inset: theoretical simulation. b) LDI-MS spectrum (positive ion mode) for the $Mn^{IV}(^{18}O)(TBP_8Cz^{\bullet+})$ fragment of $Mn^{IV}(^{18}O)(TBP_8Cz^{\bullet+}):Zn^{II}$ showing the isotope distribution pattern which corresponds to 40% incorporation of $^{18}O$. Inset: theoretical simulation. c) EI-MS spectrum of the isolated $^{18}OPPh_3$ extracted ($CH_3OH$) from the reaction of the sample in (b) + $PPh_3$ (10 equiv). A total of 88% incorporation of $^{18}O$ was observed.

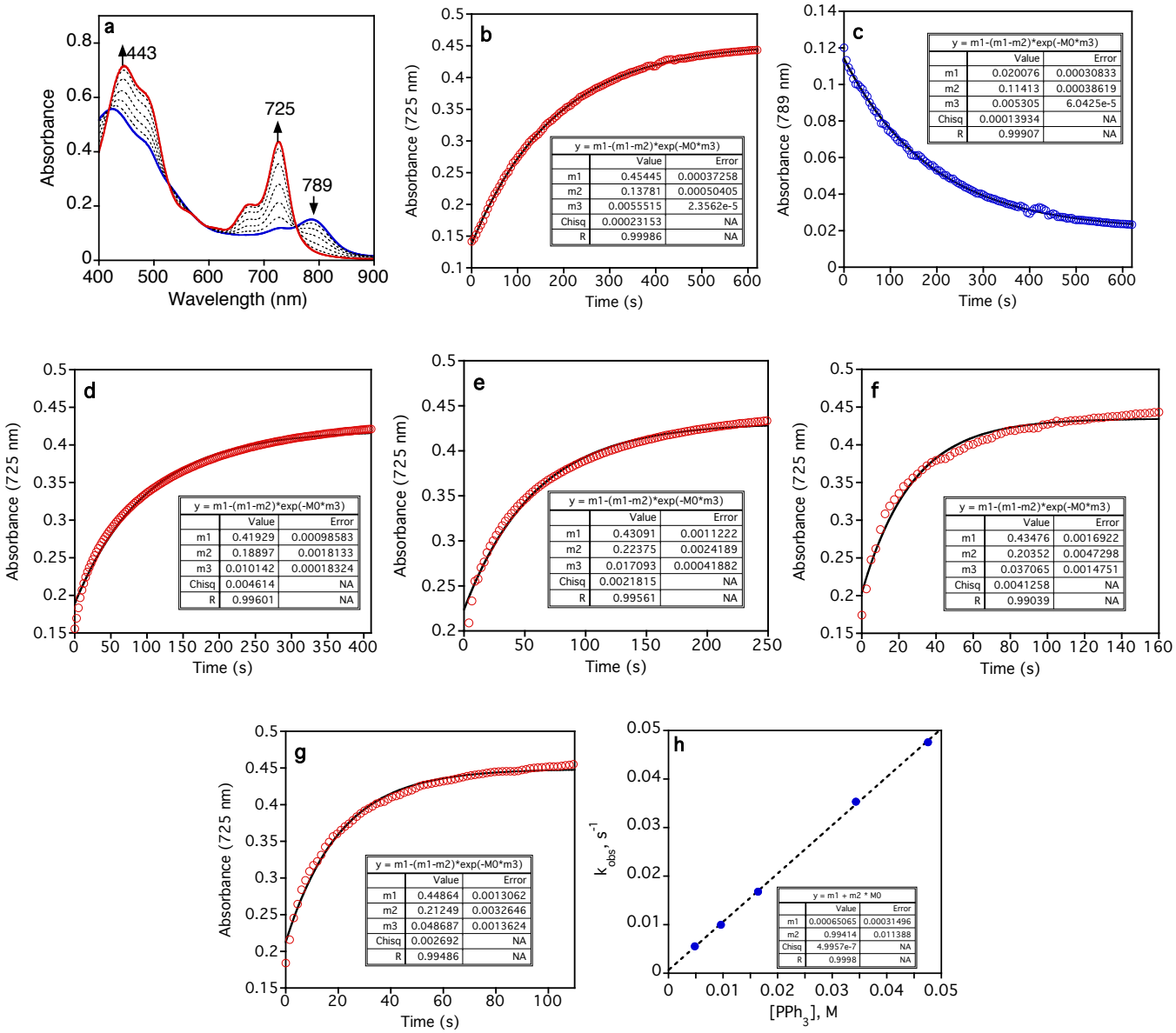


**Figure S8.** a) Representative UV-vis spectral changes (0-600 s) for the reaction of $Mn^{IV}(O)(TBP_8Cz^{\bullet+})$:$Zn^{II}$ (13 μM) (blue line) and $PPh_3$ (0.005 M) forming $Mn^{III}(TBP_8Cz)$:$Zn^{II}$ (red line) in 100:1 v/v $CH_2Cl_2/CH_3CN$ at 25˚C. b) Changes in absorbance at 725 nm over time following the growth of $Mn^{III}(TBP_8Cz)$:$Zn^{II}$. c) Changes in absorbance at 789 nm over time following the decay of $Mn^{IV}(O)(TBP_8Cz^{\bullet+})$:$Zn^{II}$. (d-g) Changes in absorbance at 725 nm over time for the production of $Mn^{III}(TBP_8Cz)$:$Zn^{II}$ after addition of varying amounts of $PPh_3$: d) 0.010 M, e) 0.016 M, f) 0.034 M, and g) 0.047 M. h)Plot of $k_{obs}$ versus [$PPh_3$].

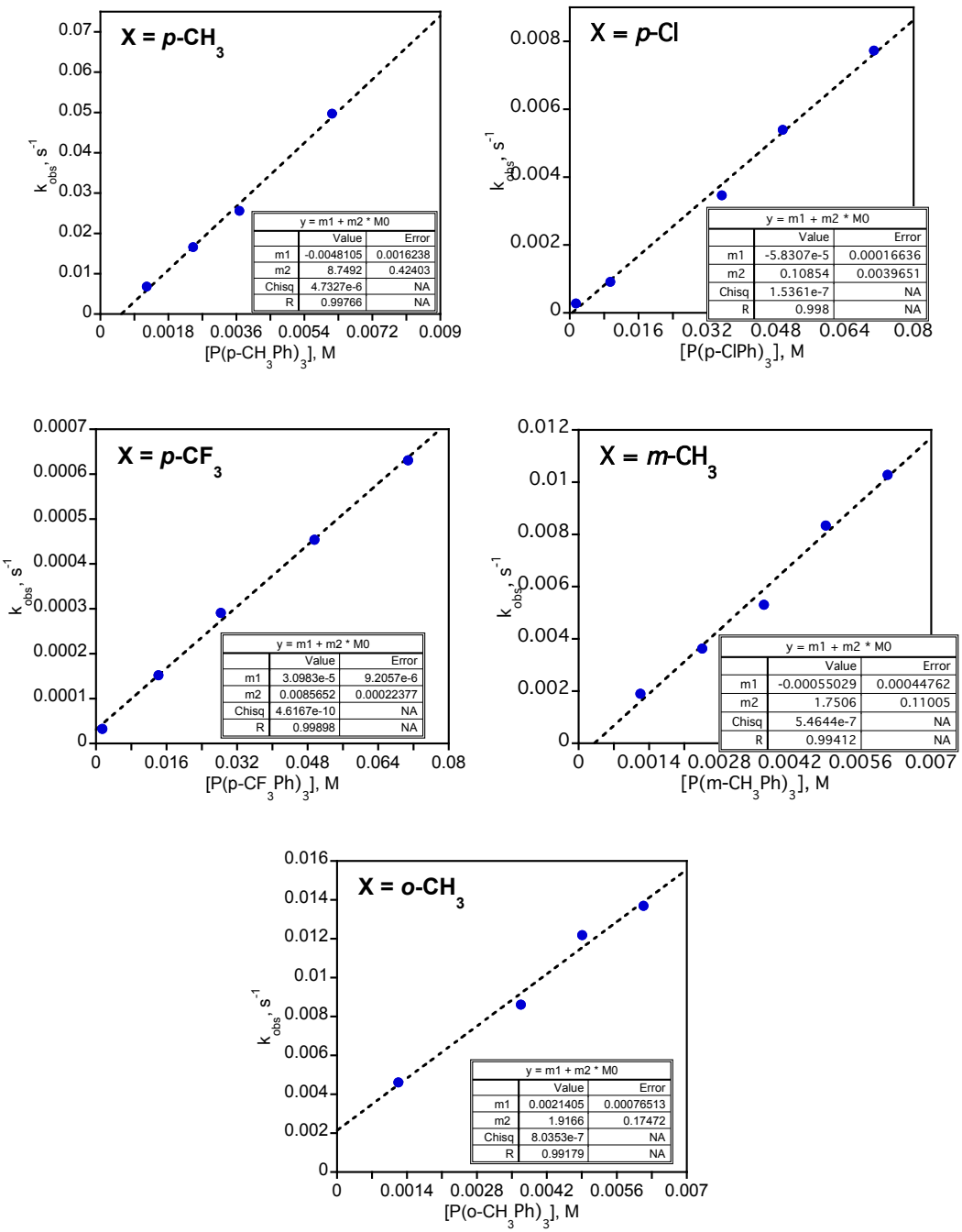


**Figure S9.** Plots of $k_{obs}$ versus $[P(X\text{-}Ph)_3]$ for the reaction of $Mn^{IV}(O)(TBP_8Cz^{\bullet+})$:$Zn^{II}$ (13 μM) in 100:1 v/v $CH_2Cl_2/CH_3CN$ at 25˚C with substituted triarylphosphines: X = *p*-$CH_3$ (0.001 – 0.006 M), *p*-Cl (0.001 – 0.07 M), *p*-$CF_3$ (0.001 – 0.07 M), *m*-$CH_3$ (0.001 – 0.006 M), *o*-$CH_3$ (0.001 – 0.006 M).

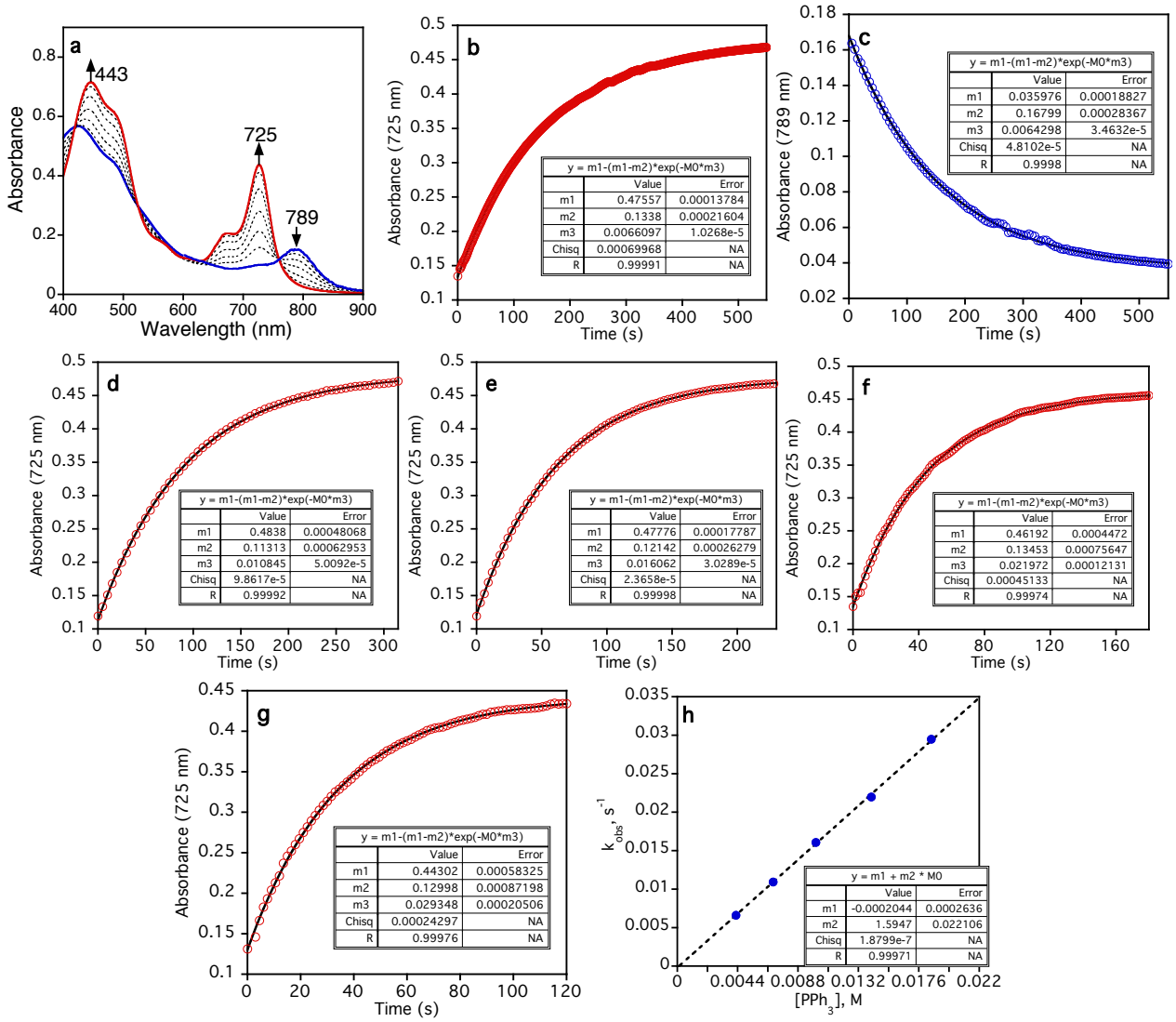


**Figure S10.** a) Representative UV-vis spectral changes (0-600 s) for the reaction of $Mn^{IV}(O)(TBP_8Cz^{\bullet+}):B(C_6F_5)_3$ (13 μM) (blue line) and $PPh_3$ (0.004 M) forming $Mn^{III}(TBP_8Cz):B(C_6F_5)_3$ (red line) in $CH_2Cl_2$ at 25˚C. b) Changes in absorbance at 725 nm over time following the growth of $Mn^{III}(TBP_8Cz):B(C_6F_5)_3$. c) Changes in absorbance at 789 nm over time following the decay of $Mn^{IV}(O)(TBP_8Cz^{\bullet+}):B(C_6F_5)_3$. Changes in absorbance at 725 nm over time for the production of $Mn^{III}(TBP_8Cz):B(C_6F_5)_3$ after addition of varying amounts of $PPh_3$: d) 0.007 M, e) 0.01 M, f) 0.014 M, and g) 0.0185 M. h)Plot of $k_{obs}$ versus [$PPh_3$].

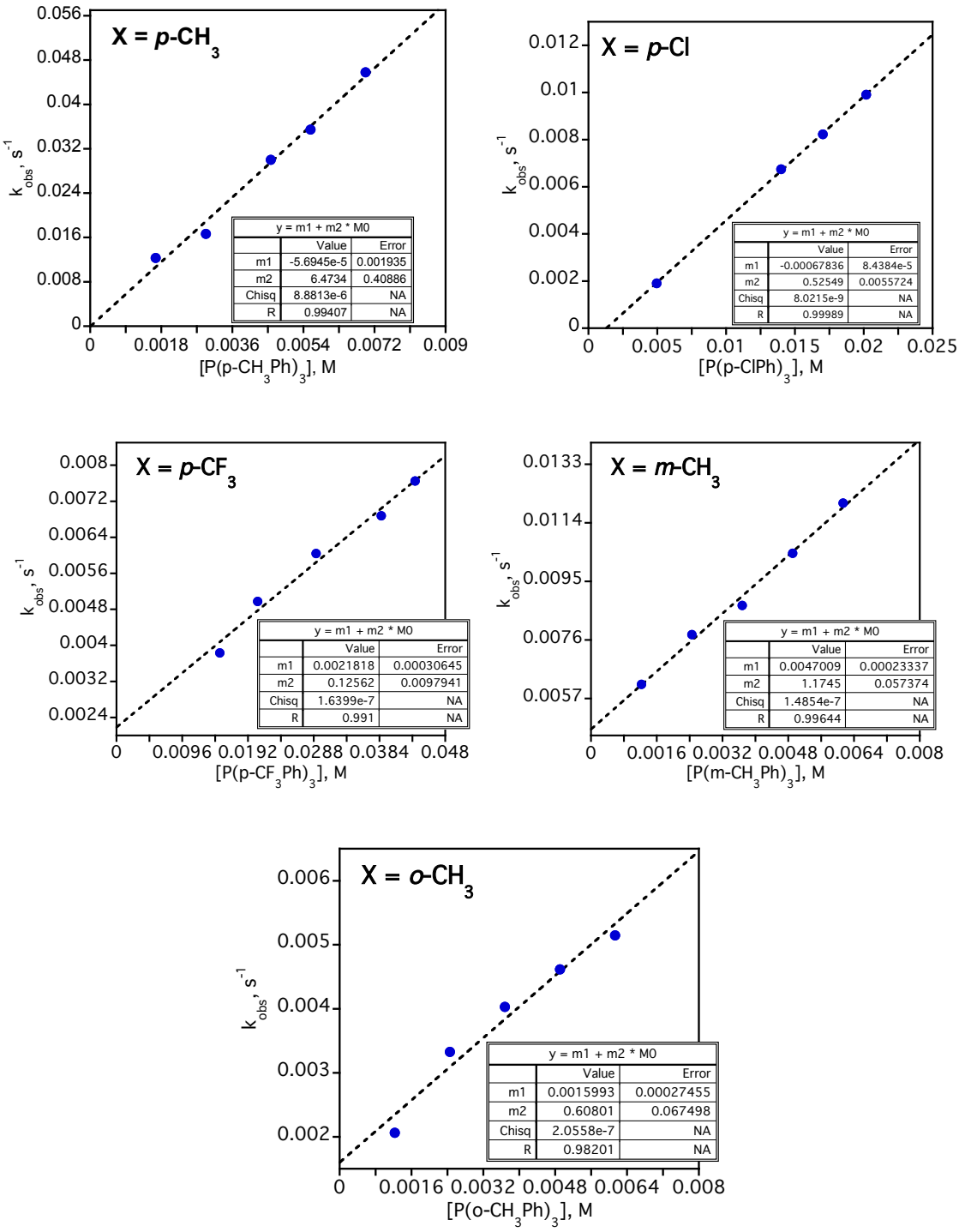


**Figure S11.** Plots of $k_{obs}$ versus $[P(X\text{-}Ph)_3]$ for the reaction of $Mn^{IV}(O)(TBP_8Cz^{\bullet+})$:$B(C_6F_5)_3$ (13 μM) in $CH_2Cl_2$ at 25˚C with substituted triarylphosphines: X = *p*-$CH_3$ (0.0017 – 0.007 M), *p*-Cl (0.005 – 0.02 M), *p*-$CF_3$ (0.015 – 0.043 M), *m*-$CH_3$ (0.001 – 0.006 M), *o*-$CH_3$ (0.001 – 0.006 M).

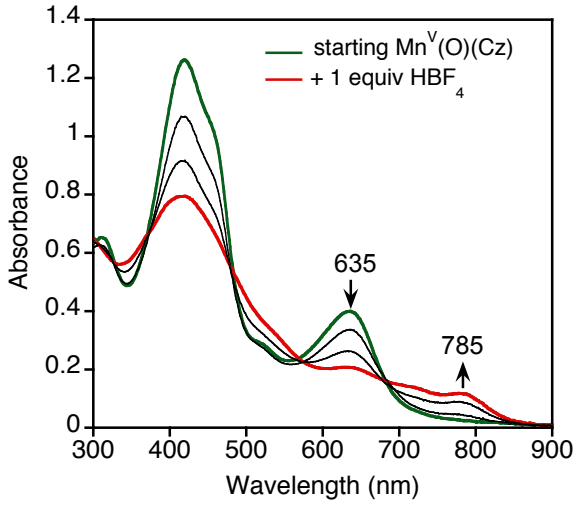


**Figure S12.** UV-vis spectra of $Mn^{V}O(TBP_8Cz)$ (20 μM) before (green line) and after (red line) the addition of $HBF_4 \bullet Et_2O$ (1 equiv) in $CH_2Cl_2$ at 25 °C. The red spectrum is assigned as $Mn^{IV}O(TBP_8Cz^{\bullet+}):H^+$.

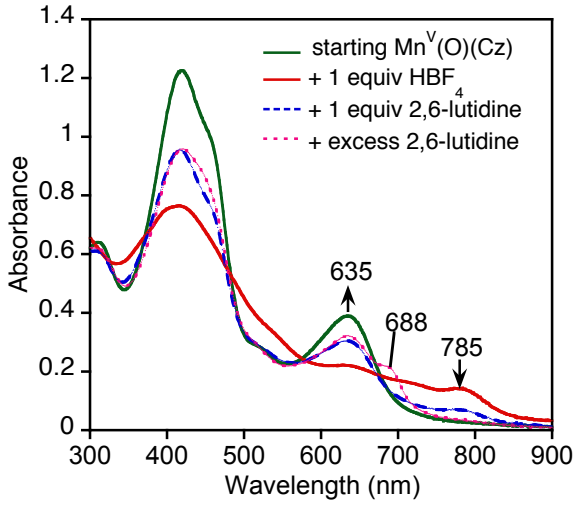


**Figure S13.** UV-vis spectra of recovery of $Mn^{V}O(TBP_8Cz)$ by addition of 2,6-lutidine in $CH_2Cl_2$ at 25 °C. $Mn^{IV}O(TBP_8Cz^{\bullet+}):H^+$ (20 μM) (red line), after addition of 2,6-lutidine (1 equiv), leads to a partially (~75 %) recovered $Mn^{V}O(TBP_8Cz)$ (dotted blue line). Addition of excess 2,6-lutidine (1000 equiv) leads to formation of a $Mn^{III}(TBP_8Cz)$ product (dotted pink line).

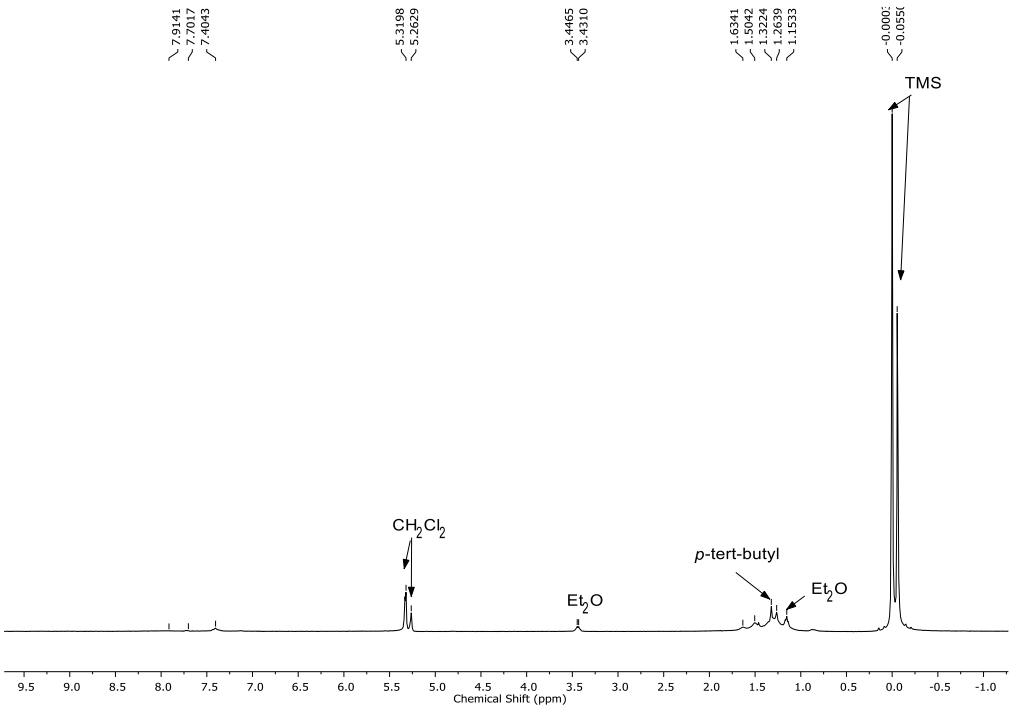


**Figure S14.** Evans method $^1$H NMR spectrum of $Mn^{IV}O(TBP_8Cz^{\bullet+})$:$H^+$ (2.0 mM) with 0.5% TMS in $CD_2Cl_2$ at 297 K. $\Delta\nu$(TMS) = 22 Hz.

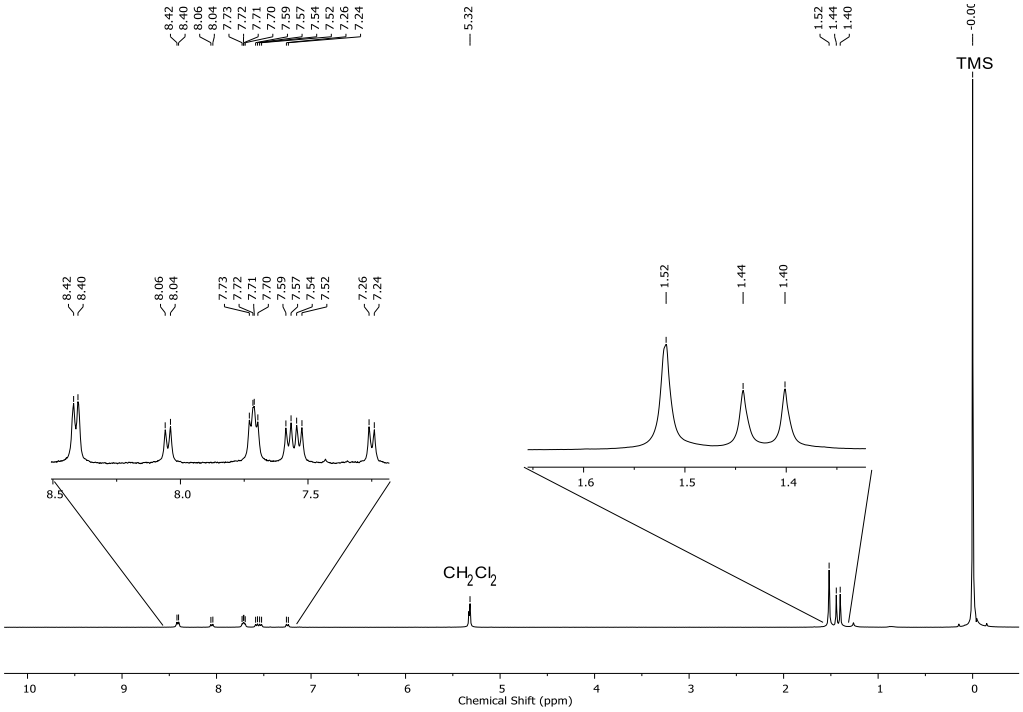


**Figure S15.** Evans method $^1$H NMR spectrum of $Mn^{V}O(TBP_8Cz)$ (2.0 mM) with 0.5% TMS in $CD_2Cl_2$ at 297 K. No shift in the TMS peak was observed.

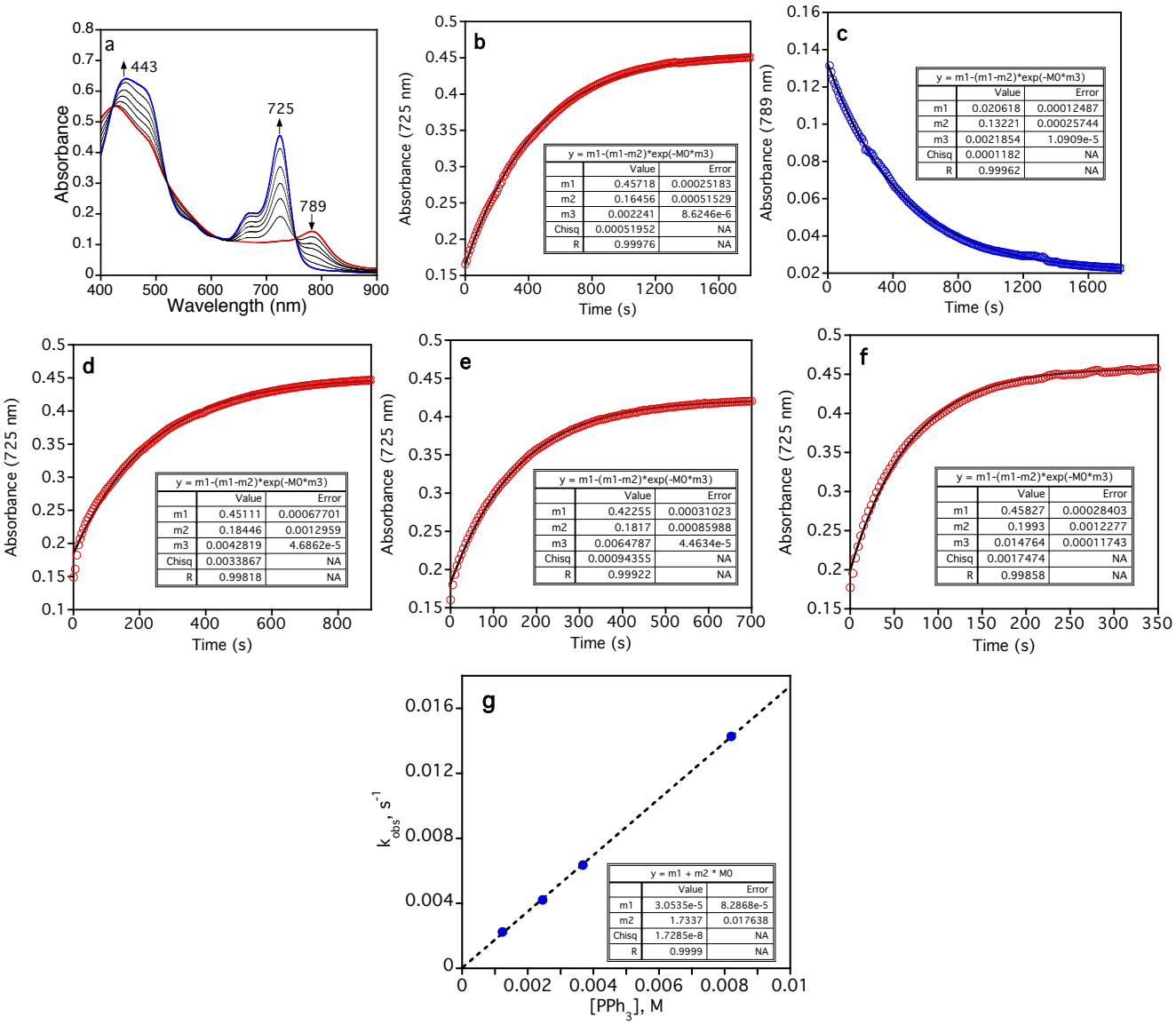


**Figure S16.** a) Representative UV-vis spectral changes (1700 s) for the reaction of $Mn^{IV}(O)(TBP_8Cz^{\bullet+}):H^+$ (13 μM) (blue line) and $PPh_3$ (0.0012 M) forming $Mn^{III}(TBP_8Cz):H^+$ (red line) in $CH_2Cl_2$ at 25˚C. b) Changes in absorbance at 725 nm over time following the growth of $Mn^{III}(TBP_8Cz):H^+$. c) Changes in absorbance at 789 nm over time following the decay of $Mn^{IV}(O)(TBP_8Cz^{\bullet+}):H^+$. Changes in absorbance at 725 nm over time for the production of $Mn^{III}(TBP_8Cz):H^+$ after addition of varying amounts of $PPh_3$: d) 0.0024 M, e) 0.0036 M, and f) 0.0082 M. g)Plot of $k_{obs}$ versus [$PPh_3$].

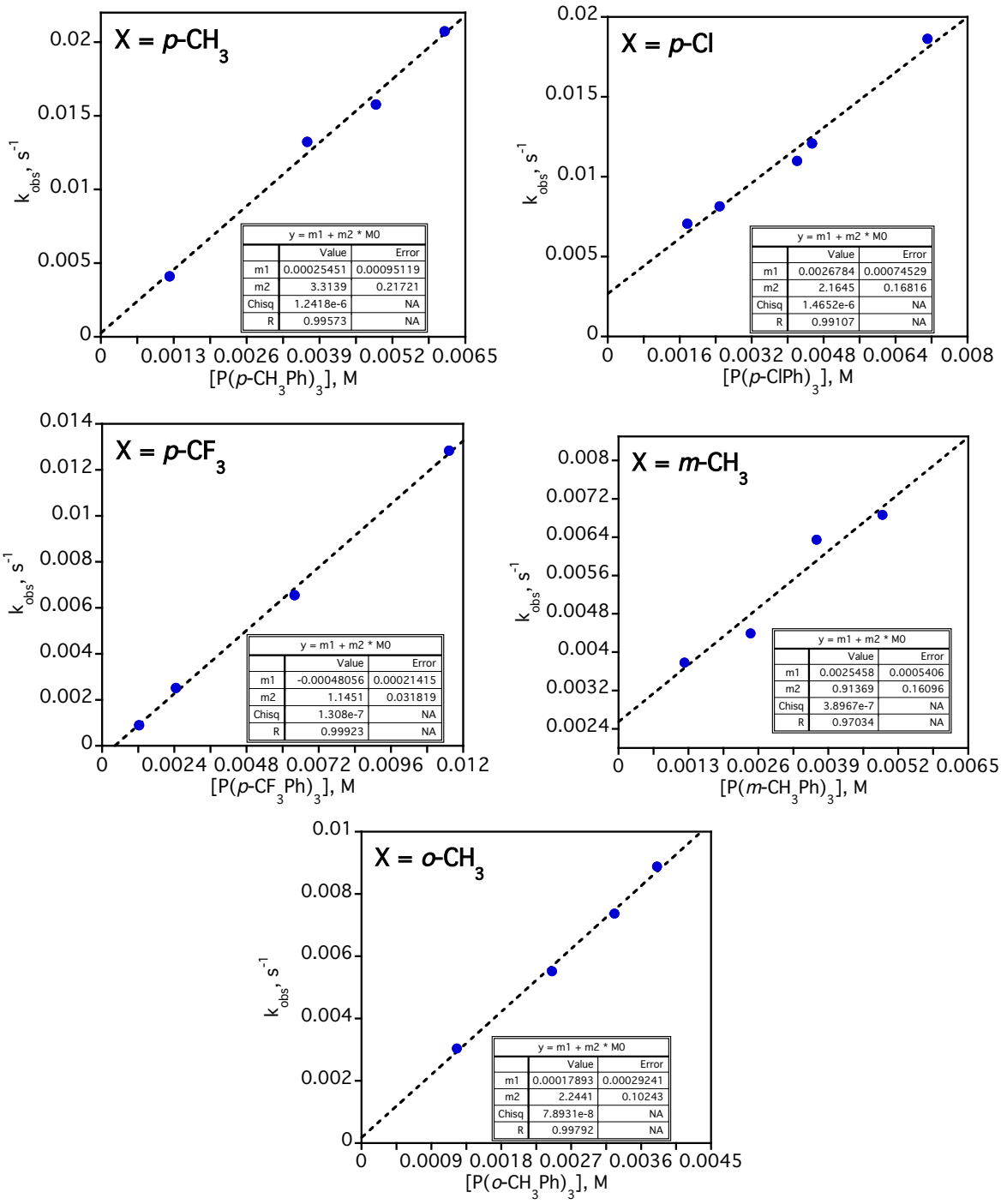


**Figure S17.** Plots of $k_{obs}$ versus $[P(X\text{-}Ph)_3]$ for the reaction of $Mn^{IV}(O)(TBP_8Cz^{\bullet+})$:$H^+$ (13 μM) in $CH_2Cl_2$ at 25°C with substituted triarylphosphines: X = *p*-$CH_3$ (0.0017 – 0.007 M), *p*-Cl (0.005 – 0.02 M), *p*-$CF_3$ (0.015 – 0.043 M), *m*-$CH_3$ (0.001 – 0.006 M), *o*-$CH_3$ (0.001 – 0.006 M).

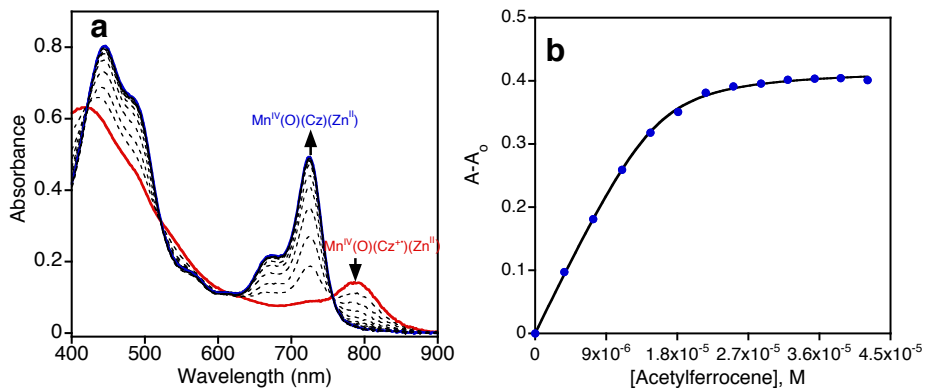


**Figure S18**. a) UV-vis spectral changes upon addition of acetylferrocene (0 – 2.25 equiv) to a solution of $Mn^{IV}(O)(TBP_8Cz^{\bullet+})$:$Zn^{II}$ (15 μM) (red line) in 100:1 $CH_2Cl_2/CH_3CN$, forming $Mn^{IV}(O)(TBP_8Cz)(Zn^{II})$ (blue line) at 25˚C. b) Plot of changes in absorbance $A-A_0$ at 725 nm upon addition of small amounts of acetylferrocene.

The plot from Figure S18b was fitted by using equation S3, which was derived as follows:

$$Mn^{IV}(O)(Cz^{\bullet+})(Zn^{II}) + AcFc \rightleftharpoons Mn^{IV}(O)(Cz)(Zn^{II}) + AcFc^{+}$$

$$K_{ET} = \frac{[Mn^{IV}(O)(Cz)(Zn^{II})]\,[AcFc^{+}]}{[Mn^{IV}(O)(Cz^{\bullet+})(Zn^{II})]\,[AcFc]} \qquad (S1)$$

$$[Mn^{IV}(O)(Cz)(Zn^{II})] = \frac{A - A_0}{\varepsilon(Mn^{IV}(O)(Cz)(Zn^{II})) - \varepsilon(Mn^{IV}(O)(Cz^{\bullet+})(Zn^{II}))} \qquad (S2)$$

Equation S3 is derived from equations S1 and S2, where $[Mn^{IV}(O)(Cz)(Zn^{II})] = [AcFc^{+}]$, $[Mn^{IV}(O)(Cz^{\bullet+})(Zn^{II})]_0 = [Mn^{IV}(O)(Cz^{\bullet+})(Zn^{II})] + [Mn^{IV}(O)(Cz)(Zn^{II})]$, and $[AcFc]_0 = [AcFc] + [AcFc^{+}]$.

$$(A - A_0) = \frac{X(Y + [AcFc]_0) - \sqrt{[X(Y + [AcFc]_0)]^2 - (4XY(X-1)[AcFc]_0)}}{2(X-1)/Z} \qquad (S3)$$

where A = absorbance throughout the titration; $A_0$ = initial absorbance; X = $K_{ET}$ = equilibrium constant of electron transfer; Y = $[Mn^{IV}(O)(Cz^{\bullet+})(Zn^{II})]_0$ = initial concentration of $Mn^{IV}(O)(TBP_8Cz^{\bullet+})(Zn^{II})$; Z = Δε =

difference in molar absorptivities between $Mn^{IV}(O)(TBP_8Cz)(Zn^{II})$ and $Mn^{IV}(O)(TBP_8Cz^{\bullet+})(Zn^{II})$ at 725 nm; $[AcFc]_0$ = initial concentration of AcFc. The plot of $A-A_0$ versus $[AcFc]_0$ was fit to eq S3 using the software Kaleidagraph 4.1.3 through a non-linear least-squares fitting routine in which X, Y, and Z were fitted variables.